Materials Today Communications 25 (2020) 101573

Contents lists available at ScienceDirect

Materials Today Communications

journal homepage: www.elsevier.com/locate/mtcomm

Optical and photocatalytic properties of ZnO and ZnS structures formed as controlled calcination products of L-cysteine assisted aqueous precipitation

Selin Şen, Ayben Top*

Department of Chemical Engineering, İzmir Institute of Technology, Urla-İzmir, 35430, Turkey

ARTICLE INFO

Keywords:
Zinc oxide
Zinc sulfide
PL spectroscopy
Intrinsic defects
Photocatalytic degradation

ABSTRACT

ZnO and ZnS structures were obtained by the calcination of the aqueous precipitation products of $Zn(NO_3)_2$, NaOH and L-cysteine (Cys). Initial Cys:Zn molar ratios were changed as 0.1:1, 0.5:1, 1:1 and 1.5:1. All the precursors were transformed into ZnO upon calcination at 700 °C. ZnS structures were obtained by calcining the precursors prepared at the Cys:Zn ratios of 1 and 1.5 at 350 °C. In addition to changing chemical composition of the precipitation products, calcination temperature and initial Cys:Zn ratio also affected morphology, surface area, photoluminescence and photocatalytic properties of the final products. Free exciton energy values of the ZnO samples were observed to be between 3.29 eV and 3.35 eV. PL spectra of the ZnO samples indicated blue and green emission centers. Zinc interstitials (Zn_i), revealed by the blue emissions in the PL spectra were also confirmed by Auger Zn $L_3M_{4.5}M_{4.5}$ spectra. The samples calcined at 350 °C removed rhodamine B mainly by adsorption. All the samples calcined at 700 °C successfully degraded the dye under UV light. Among the samples calcined at 700 °C, ZnO sample prepared at Cys:Zn = 0.5, which has the highest surface area and unique photoluminescence spectrum exhibited the fastest photodegradation rate.

1. Introduction

Generation of large amounts of organic pollutants such as dyes, pharmaceuticals, surfactants and fertilizers is one of the inevitable consequences of the population growth and continuous industrial and agricultural development. Contamination of water resources by these wastes causes hazardous effects to the human health and balance of the ecosystems. Thus, life-threatening effects of water pollution along with the environmental regulations and limitation of water resources necessitate the treatment of the polluted effluents [1–7]. Among many wastewater treatment methods including adsorption, membrane separation and coagulation, advanced oxidation processes have been proposed for the elimination of the persistent organic pollutants, especially for the ones with low biodegradability. Advanced oxidation processes are based on the generation of highly reactive radicals by using ozone (O_3), hydrogen peroxide (H_2O_2), Fenton's reagent, UV light or a semiconductor catalyst. These radicals, then, convert the organic pollutants to less toxic compounds [8,9].

In the case of semiconductor catalysts, radical generation is triggered via photons. Basically, semiconductor catalysts absorb the photons having energy greater than band gap energies of the semiconductors by generating holes in the valence band (VB) and electrons in the conduction band (CB). These photogenerated holes and electrons react with water, hydroxyls and dissolved oxygen to form the radical species capable of degradation of the pollutants [10,11]. Although semiconductor based photocatalytic degradation processes are clean, environmentally friendly and sustainable, photocatalytic reaction rates are generally not fast enough to be employed in high throughput processes [2,12]. Therefore, correlations between properties and photocatalytic activities of semiconductors should be well exploited for the preparation of novel photocatalysts, practically applicable in the treatment of the industrial effluents.

Photocatalytic performance of the semiconductors is a complex phenomenon controlled mainly by their electronic and surface properties [12]. Defects [13–15] and morphology [16–18] were also reported to affect photocatalytic activities of the semiconductor photocatalysts. Additionally, as the size of the semiconductors decreases to nanoscale, they exhibit exclusive characteristics such as high surface area and highly reactive surface, which promote photocatalytic abilities of the semiconductors [19,20].

Zinc based semiconductors, ZnO and ZnS, with wide band gaps in the near-UV spectral region have been mostly considered for electronic, photovoltaic and optoelectronic applications [21–26]. Moreover, ZnO and ZnS have also been demonstrated as promising heterogeneous photocatalyst candidates alternative to TiO_2 based semiconductors [12,27–30]. For example, photo-induced water splitting properties of

* Corresponding author.
E-mail address: aybentop@iyte.edu.tr (A. Top).

https://doi.org/10.1016/j.mtcomm.2020.101573
Received 13 February 2020; Received in revised form 13 August 2020; Accepted 14 August 2020
Available online 22 August 2020

ZnS were reported [31–34]. Also, ZnO having antifouling and antibacterial properties was proposed as an effective photocatalyst in water treatment [8,35–39]. Although band gap energy of ZnO is close to that of TiO_2, ZnO has higher absorption efficiency and lower production cost compared to TiO_2 [8,40]. Additionally, superior to TiO_2, zinc-based semiconductors can be synthesized via a variety of synthesis routes including precipitation [41], sol-gel [42], hydrothermal [43], solvothermal [44], pulsed laser ablation [45] and chemical vapor deposition [46] methods.

Aqueous precipitation is a simple and environmentally benign method for the preparation of zinc based semiconductors. Besides, utilization of different additives in this method coupled with the availability of various post-synthesis treatment options allows the synthesis of materials with different characteristics. In this study, it was aimed to determine photocatalytic activities of zinc based semiconductors with different structural and optical properties synthesized via aqueous precipitation route followed by calcination process.

We synthesized precursors of the zinc based semiconductors by employing L-cysteine as an additive in the aqueous precipitation method. The precursors were prepared by using different Cys:Zn ratios. Then, these samples were calcined at different temperatures to control the chemical composition of the final products. We showed that L-cysteine can be used as a sulfur source in the preparation of ZnS samples when appropriate Cys:Zn ratios and calcination temperature are used. In addition to changing chemical composition of the zinc based semiconductors, Cys:Zn ratio and calcination temperature also alter morphology, surface area and optical properties of these products. Finally, effects of these chemical and physical properties of the Zn based semiconductors on their photocatalytic activities were discussed.

2. Materials and methods

2.1. Materials

Zinc nitrate hexahydrate ($Zn(NO_3)_2.6H_2O$, Riedel de Haen, > 98 %), sodium hydroxide (NaOH, Sigma-Aldrich, 98–100.5 %), and L-cysteine (Aldrich, > 97 %) were used in the preparation of the precursors. Rhodamine B (dye content ≥ 90 %) and FTIR grade potassium bromide (≥ 99 %) were purchased from Merck and Sigma-Aldrich, respectively. In all solution preparations and washing processes, deionized water was employed. Pure terephthalic acid (TA) kindly supplied by Petkim Petrochemical Co. (İzmir, Turkey) was used in the detection of hydroxyl radicals.

2.2. Sample preparation

The precursors were prepared by adding 120 mL 0.2 M NaOH solution (0.96 *g* NaOH/120 mL) into equal volume of 0.1 M Zn $(NO_3)_2.6H_2O$ solution (3.57 *g* $Zn(NO_3)_2.6H_2O$/120 mL) containing L-cysteine. Molar ratios of Cys to Zn were changed as 0.1:1, 0.5:1, 1:1 and 1.5:1 by using 0.145, 0.727, 1.454 and 2.181 *g* L-cysteine, respectively. The as-synthesized samples (precursors) are referred to as CZ-0.1, CZ-0.5, CZ-1 and CZ-1.5 according to the Cys:Zn ratio used in their preparations. Similarly, the sample code, CZ-0, is assigned to the sample synthesized without L-cysteine. The solutions were stirred at room temperature for overnight. The precipitates formed were collected by centrifugation. They were washed with deionized water, and were dried in a vacuum oven at 40 °C. The dried precipitates were calcined at 350 °C or 700 °C for 2 h. The calcined samples are denoted as CZ-X-Y where X is the Cys:Zn ratio and Y is the calcination temperature.

2.3. Characterization

Powder X-ray diffraction (XRD) experiments were carried out using a Philips Xpert-Pro (Panalytical, Almelo, Netherlands) diffractometer with an incident CuK_α radiation at 1.54 Å. Fourier transformed infrared (FTIR) spectra of the samples were obtained by using KBr disk technique. The spectra were taken on an FTIR-8400S (Shimadzu, Kyoto, Japan) spectrophotometer with 2 cm^{-1} resolution. Scanning electron microscopy (SEM) images of the samples were obtained using an FEI Quanta 250 FEG (FEI Company, Hillsboro, OR) model instrument. Thermal gravimetric analyses (TGA) of the samples were performed by using a TGA-51 (Shimadzu, Kyoto, Japan) system. In these experiments, the samples were heated from room temperature to 1000 °C with a heating rate of 10 °C/min under nitrogen atmosphere. Nitrogen physisorption measurements were used to determine Brunauer, Emmett and Teller (BET) surface area values of the samples. These experiments were carried out using an ASAP 2010 (Micromeritics, Norcross, GA) model static volumetric adsorption equipment. UV–vis spectra of the calcined samples dispersed in ethanol were obtained by employing a UV-2450 (Shimadzu, Kyoto, Japan) model spectrophotometer. Photoluminescence (PL) spectra of the powder samples were taken using LS-55 model fluorescence spectrophotometer (Perkin Elmer, Waltham, MA) equipped with a front surface accessory. Excitation wavelengths were used as 325 nm and 275 nm for the ZnO samples and the other samples, respectively. X-ray photoelectron spectroscopy (XPS) of the samples was performed on a Thermo Scientific K-Alpha X-ray photoelectron spectrometer. X-band electron paramagnetic resonance (EPR) spectroscopy experiments were carried out using a CMS 8400 Adani model benchtop spectrometer at room temperature.

2.4. Photocatalytic degradation experiments

Rhodamine B (RhB) was used as a model dye to evaluate photocatalytic activities of the calcined samples. First, a dye stock solution with a concentration of 1×10^{-5} M was prepared by using the molar extinction coefficient of RhB at 554 nm, 8.8×10^4 cm mol^{-1} L^{-1} [47]. 50 mL stock solution was treated with 50 mg sample in dark for 1.5 h to establish the adsorption equilibrium between the dye molecules and the sample. Then, the solution was irradiated with a UV light source (Osram dulux S blue UVA, 2 × 9 W) for 2 h. During the adsorption and the UV irradiation periods, 0.5 mL aliquots were withdrawn at definite time intervals and were centrifuged at 8000 rpm for 3 min to separate particulate matter. Absorbance values of the dye solutions were measured at 554 nm using a Shimadzu UV-2450 model UV–vis spectrophotometer. C_o/C values used in the kinetic analyses were calculated by using the Beer-Lambert law as follows:

$$\frac{C_o}{C} = \frac{A_o}{A} \quad (1)$$

where A_o, A, C_o, and C are initial absorbance, absorbance value measured at time t, initial dye concentration, and dye concentration at time t, respectively.

Formation of hydroxyl radicals on the surface of select samples exposed to UV irradiation was monitored using TA as a probe molecule, which reacts with hydroxyl radicals to form photoluminescent 2-hydroxyterephthalic acid (HTA) [48]. In these experiments, 15 mg sample was dispersed in 15 mL of 5×10^{-4} M TA prepared in aqueous solution of 2×10^{-3} M NaOH and the mixture was stirred in dark at least for an hour. Then, the mixture was exposed to the UV lamps used in the RhB degradation experiments. Aliquots were withdrawn and were centrifuged. PL spectra of HTA in the supernatants were recorded as a function of irradiation time. The measurements were performed on a Perkin Elmer LS-55 model fluorescence spectrophotometer by using an excitation wavelength of 315 nm.

3. Results and discussion

3.1. Structural and thermal characterization

Crystal structures of the as-synthesized and the calcined products were investigated using XRD analysis. XRD patterns of the samples

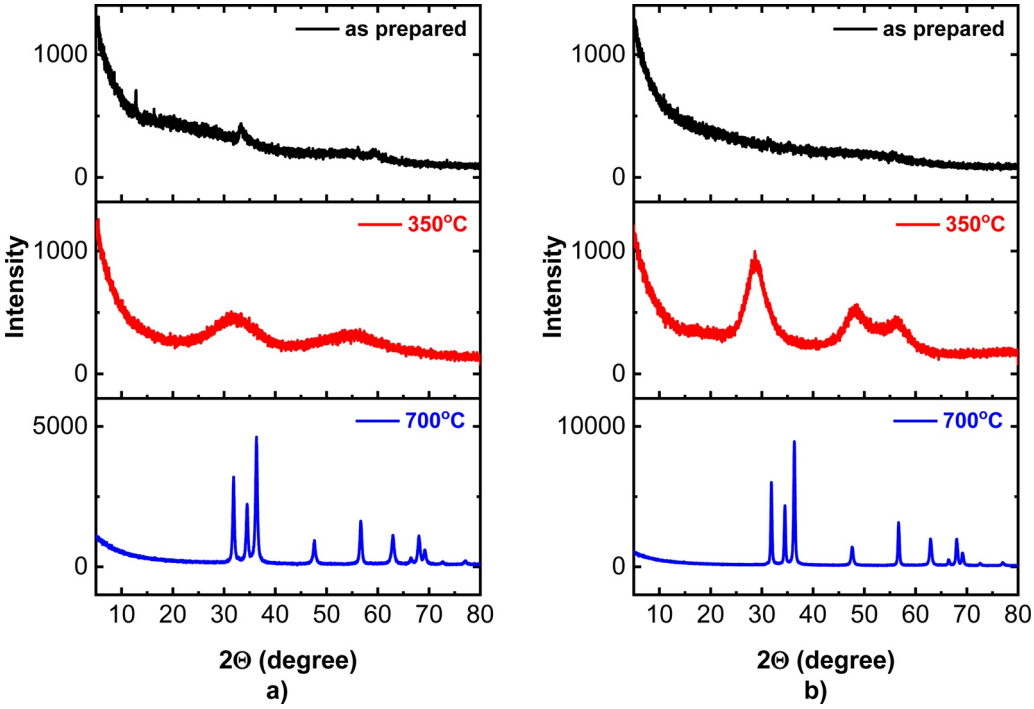

Fig. 1. XRD patterns of the samples prepared at Cys:Zn ratio of a) 0.5 and b) 1.

prepared at Cys:Zn molar ratios of 0.1, 0.5, 1 and 1.5 are given in Figs. S1a, 1a, 1b and S1b, respectively. Among as-synthesized samples, CZ-0.5, CZ-1 and CZ-1.5 did not show any diffraction peaks indicating amorphous nature of these samples. CZ-0.1, on the other hand, exhibited diffraction peaks with 2θ values of 15.3, 15.8, 19.0, 20.8, 26.0, 26.9, 27.8, 28.8, 29.6, 30.9, 31.6, 33.3, 34.2, 35.8, 36.9, 38.5, 39.0, 40.9, 47.2, 48.2 and 49.2 degrees. This pattern matches to the XRD peaks of a β-$Zn(OH)_2$ structure with a PDF card number of 20–1435 except missing peaks at 17.1, 21.4 and 32.4 degrees, which correspond to (112), (114) and (217) planes, respectively.

Fig. 1 and Fig. S1 also indicate that crystal structures of the calcined samples are determined by both Cys:Zn ratio and calcination temperature. CZ-0.1 − 350 and all the samples calcined at 700 °C formed wurtzite type ZnO structure (PDF card number = 80 − 0074). However, in the XRD spectra of CZ-1 − 350 and CZ-1.5 − 350, three broad peaks centered at about 28.6 (111), 48.1 (220) and 56.2 (311) degrees were observed indicating cubic zinc blende type ZnS crystal structure (PDF card number = 05 − 0566). For these samples, the peak position associated with (220) plane shifted ~0.6 degree to the higher 2θ value compared with the peak position of (220) plane in the XRD spectrum of the standard ZnS. Interestingly, the sample CZ-0.5 − 350 has a unique XRD pattern, composed of two broad peaks at 31.8 and 55.2 degrees, which corresponds to an unfamiliar crystal structure.

Previously, we synthesized a sample in the absence of L-cysteine using the same experimental procedure as outlined in Section 2.2 and denoted the sample as C1-SA. This sample corresponds to CZ-0 in the current study. Unlike the samples synthesized in the presence of L-cysteine, C1-SA formed ε-$Zn(OH)_2$ crystal structure (PDF card number = 76–1778). Calcination of C1-SA at 700 °C yielded wurtzite type ZnO, in consistent with the results of the current study [49].

Ma et al. (2012) also employed L-cysteine to prepare N-doped ZnO/ZnS composites. The authors used higher concentration of Zn source (0.25 M) and NaOH (0.5 M) and performed calcination under nitrogen atmosphere. They observed that only the sample prepared at Cys:Zn ratio of 5 and calcined at 400 °C formed a pure zinc blende ZnS phase. At the same calcination temperature, lower Cys:Zn ratios used in the synthesis of the precursors were resulted in mixtures of ZnS and ZnO [50].

Crystallite sizes of the ZnO samples were estimated using the Scherrer equation as given below:

$$d = \frac{K\lambda}{\beta cos\theta} \quad (2)$$

where K is the Scherrer constant (0.9), λ is the X-ray wavelength (1.5406 Å), θ is the Bragg angle and β shows the full width at half maximum (FWHM) of the peak [51,52]. Using Gaussian profile, instrument broadening effect was corrected via the following equation:

$$\beta = \sqrt{\beta_{exp}^2 - \beta_{standard}^2} \quad (3)$$

where β_{exp} and $\beta_{standard}$ are the FWHM values of the sample and the standard, respectively and β is the corrected width [51]. In the calculation of β values, $\beta_{standard}$ was taken as the average FWHM of Y_2O_3 sample calcined at 1100 °C for 1 h [53]. Average crystallite sizes of the ZnO samples calculated by using corrected width values are given in Table 1. Crystallite sizes of the samples prepared in the presence of L-cysteine are lower than that of CZ-0 − 700. Both amount of L-cysteine used in the synthesis of the precursors and calcination temperature of these precursors influence the crystallite sizes of the ZnO samples.

Functional groups of the samples and qualitative estimation of L-cysteine incorporation into the precursors were assessed via FTIR

Table 1
Average crystallite sizes and BET surface area values of the calcined samples.

Sample	Cys:Zn mole ratio	Calcination temperature (°C)	Average crystallite size (nm)	BET surface area (m^2/g)
CZ-0 − 700	0	700	66 ± 7	3*
CZ-0.1 − 350	0.1	350	8 ± 2	85
CZ-0.1 − 700		700	23 ± 4	16
CZ-0.5 − 350	0.5	350	–	65
CZ-0.5 − 700		700	20 ± 3	36
CZ-1 − 350	1	350	–	19
CZ-1 − 700		700	33 ± 8	19
CZ-1.5 − 350	1.5	350	–	15
CZ-1.5 − 700		700	34 ± 7	16

* taken from Top and Çetinkaya (2015) [49].

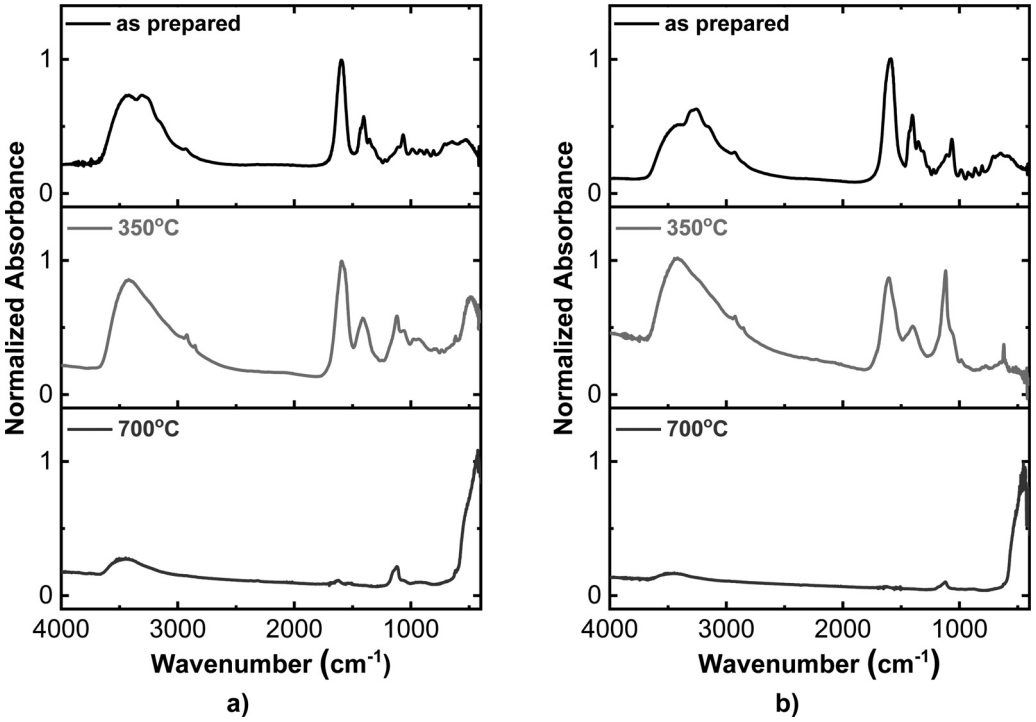

Fig. 2. FTIR spectra of the samples prepared at Cys:Zn ratio of a) 0.5 and b) 1.

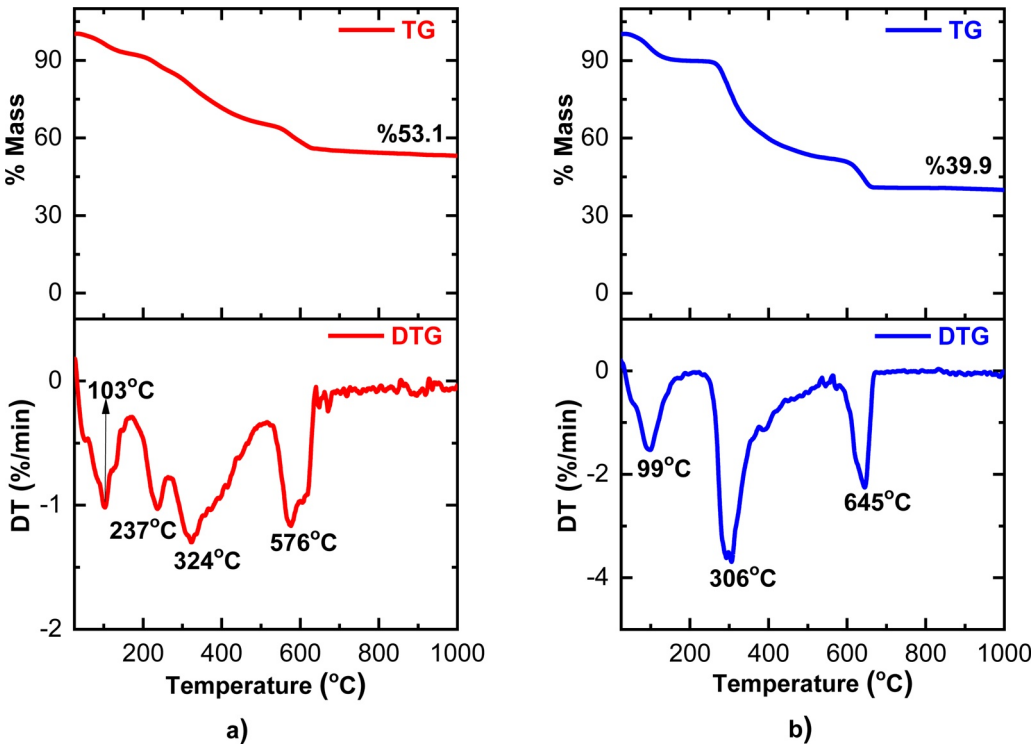

Fig. 3. TG and DTG curves of the samples a) CZ-0.5 and b) CZ-1.

spectroscopy. TGA data were used to get quantitative estimation of L-cysteine content of the precursors. FTIR spectrum and TGA curve of L-cysteine are presented in Fig. S2 and Fig. S3, respectively. Fig. S2 indicates characteristic bands of L-cysteine related to SH (2550 cm^{-1}), CO_2- (823 cm^{-1}) NH_3^+ (1065, 1347, 1585 and 3180 cm^{-1}) vibrations [54]. In its DTGA curve, L-cysteine has a major degradation peak centered at 251 °C. In this degradation step, almost 80 % of total mass of L-cysteine was converted to gaseous products.

FTIR spectra of the samples prepared at Cys:Zn ratios of 0.1, 0.5, 1 and 1.5 are shown in Figs. S4a, 2a, 2b and S4b, respectively. CZ-0.1 exhibits vibration bands associated with both $Zn(OH)_2$ and L-cysteine in its FTIR spectrum. The bands between 400 and 1200 cm^{-1} predominantly represent $Zn(OH)_2$ vibrations whereas those between 1200 − 1800 cm^{-1} are mainly because of incorporation of L-cysteine into the precursor. The band at 481 cm^{-1} indicates lattice Zn-O vibrations. Additionally, asymmetric stretching vibrations of Zn-O-Zn

were observed at 1040 and 1075 cm^{-1} [55,56]. At higher Cys:Zn ratios, intensities of the bands between 1200 and 1800 cm^{-1} increase relative to those of the bands observed at lower wavenumbers. Presence of L-cysteine in the as-synthesized samples was also confirmed by a band at ~2920 – 2930 cm^{-1}, which corresponds to C–H stretching vibrations. FTIR spectra of CZ-1 – 350 and CZ-1.5 – 350 indicate mainly adsorbed and oxidized species on ZnS surface and degradation products of L-cysteine as Zn-S-Zn vibrations are observed at about 350 cm^{-1} [57]. Mainly, the band at about 1400 – 1420 cm^{-1} is because of the formation of Zn-$OHCO_2$ complex at the surface. No peak associated with ZnS-H absorption band at ~2500 cm^{-1} was observed [57,58]. The bands at 620 cm^{-1} and 1120 cm^{-1} were proposed to be related to the oxidation products with unknown oxidation state and nature. OH stretching and H–O–H bending vibrations are identified by the bands at about 3400 cm^{-1} and 1600 – 1620 cm^{-1}, respectively [58]. FTIR spectrum of the sample, CZ-0.5 – 350, with undefined crystal structure looks like the FTIR patterns of the ZnS samples except the presence of a band at 492 cm^{-1} that corresponds to Zn-O vibrations. This band shifted to 441 cm^{-1} for the sample, CZ-0.1 – 350. Zn-O vibrations are also apparent at ~420 – 450 cm^{-1} in the FTIR spectra of all the ZnO samples calcined at 700 °C, as expected. Additionally, quite weak absorption bands at about 1120 cm^{-1} and 3400 – 3500 cm^{-1} region were observed in these spectra.

TGA and corresponding DTG curves of CZ-0.5 and CZ-1 are given in Fig. 3a and Fig. 3b, respectively. DTG curves of CZ-0.5 and CZ-1 indicate four-step and three-step mass losses, respectively. The first peak observed at about 100 °C for both samples is because of the evaporation of moisture and other volatiles in the samples. The other peaks predominantly indicate degradation of L-cysteine. The differences in the number and position of these peaks can be explained by the formation of different degradation products. Weight loss between onset and ending temperatures of the degradation peaks was used to calculate amount of L-cysteine incorporation into the precursors, roughly. Accordingly, initial L-cysteine contents were estimated as 37 % and 49 % for the samples CZ-0.5 and CZ-1, respectively.

3.2. Morphology and surface area results

SEM images of the samples are given in Fig. 4 and Fig. S5. CZ-0.1 has mixed morphology composed of plate-like structures (characteristics of β-$Zn(OH)_2$) and irregular structures (Fig. S5a) [49]. Calcination of this sample generated pores in the plate-like structures (Figs. S5b-c). Additionally, spherical structures with 20 – 40 nm diameters formed upon calcination of CZ-0.1 at 700 °C (Fig. S5c). At Cys:Zn ratio of 0.5, cauliflower-like aggregates are apparent in the SEM pictures of the precursor and the sample calcined at 350 °C as given in Fig. 4a and Fig. 4b, respectively. Spherical nanoparticles with diameters between 20 nm and 50 nm and occasional rod-like structures were obtained upon calcination of CZ-0.5 at 700 °C (Fig. 4c). Interestingly, larger well-defined spherical nanoparticles with sizes between 50 nm and 100 nm were observed for CZ-1 (Fig. 4d) and the size and morphology of these nanostructures did not change appreciably upon calcination (Figs. 4e-f). When Cys:Zn ratio was increased to 1.5, interconnected irregular morphology was observed (Figs. S5 d–e). Calcination of CZ-1.5 at 700 °C, on the other hand, yielded nanoparticles having sizes between 50 and 100 nm as revealed by Fig. S5f.

In our previous study, SEM picture of the as-synthesized sample prepared without any additive, indicated octahedral structures, typical morphology of ε-$Zn(OH)_2$ crystals [49]. Thus, plate-like, cauliflower-like, irregular and spherical structures observed in the current study clearly demonstrate morphogenic effect of L-cysteine.

BET surface area values of the calcined samples are given in Table 1. The samples with spherical morphology (CZ-0.5-700, CZ-1-700, CZ-1.5-700 and CZ-1-350) exhibit surface area values proportional to their particle sizes, as expected. The highest surface area was obtained for CZ-0.1-350 sample. Surface area values of CZ-0.1-350 and CZ-0.1-700 were determined as 85 m^2/g and 16 m^2/g, respectively. The lower surface area of CZ-0.1-700 can be explained by its higher crystallite size. Similar behavior was also observed for the calcined TiO_2 samples. Surface area of TiO_2 decreased dramatically from 190.5 m^2/g to 0.80 m^2/g, as its crystallite size increased from 9.37 nm to 60.3 nm upon calcination [59].

3.3. Optical properties

UV–vis absorption spectra of the samples calcined at 700 °C and 350 °C are given in Fig. 5 and Fig. S6, respectively. For ZnO samples, excitonic peak positions vary between 370 nm (3.35 eV) and 377 nm (3.29 eV) indicating no correlation with initial Cys:Zn ratio. These free exciton (FX) energy values of the samples are slightly lower than the free exciton energy of bulk ZnO crystals, reported as 3.377 eV [60]. For ZnS samples, CZ-1 – 350 and CZ-1.5 – 350, excitonic peaks appear at

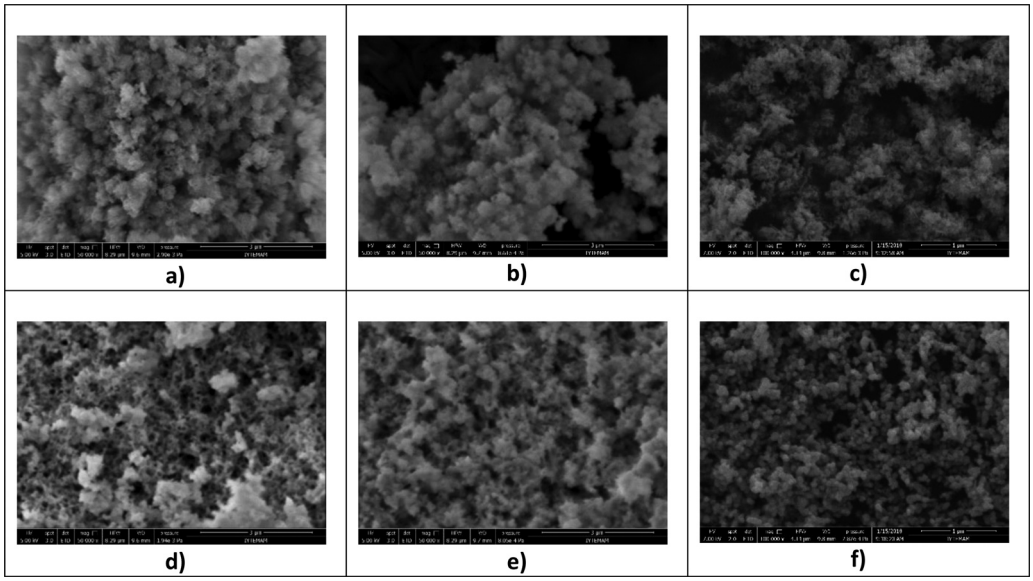

Fig. 4. SEM pictures of the samples prepared at Cys:Zn ratio of 0.5 a) as-synthesized, b) calcined at 350 °C, c) calcined at 700 °C and the samples prepared at Cys:Zn ratio of 1 d) as-synthesized, e) calcined at 350 °C, f) calcined at 700 °C (Scale bars: a, b, d, e = 3 μm; c, f = 1 μm).

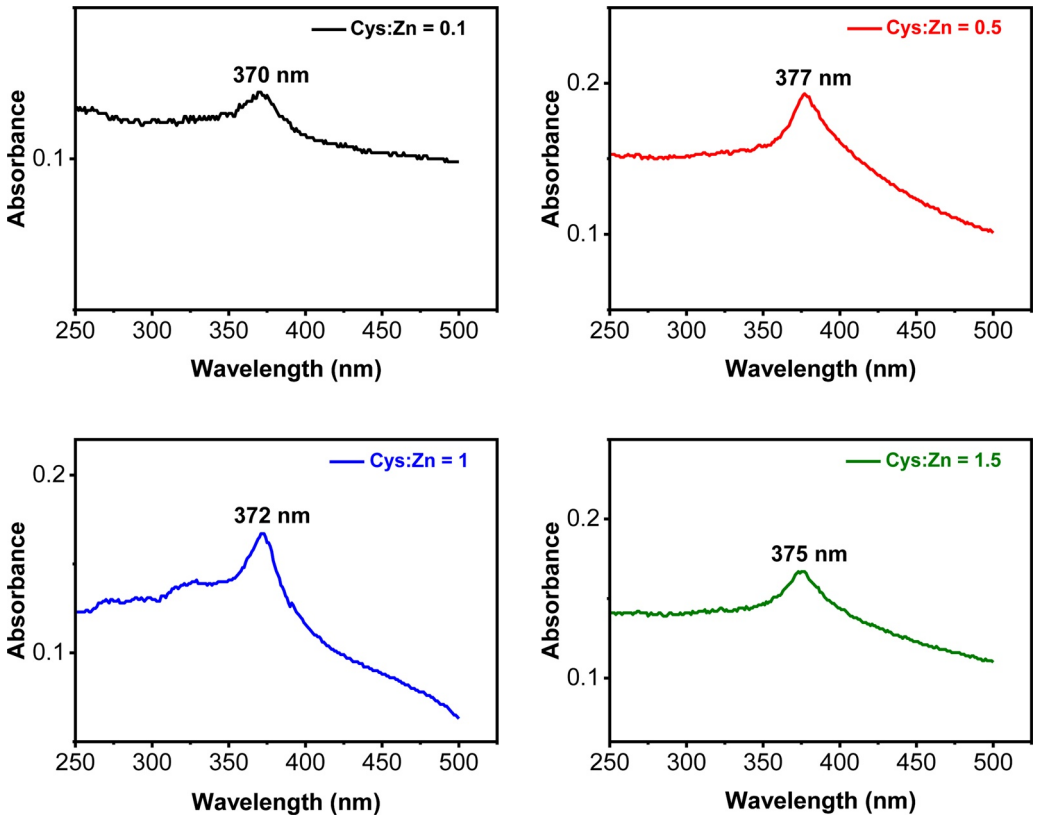

Fig. 5. UV–vis spectra of the samples calcined at 700 °C.

321 nm (3.86 eV) and 328 nm (3.77 eV), respectively. For the sample with unidentified crystal structure, CZ-0.5 − 350, the excitonic peak is blue-shifted to 304 nm (4.08 eV) in its UV spectrum.

PL spectra of the ZnO samples were taken to monitor crystal defects of these samples. The PL spectra were deconvoluted into Gaussian peaks and are given in Fig. 6 and Fig. S7. % area values of the deconvoluted peaks of the PL spectra are given in Table 2. PL spectrum of each sample was fitted to five Gaussian peaks with small shifts in the peak positions. The first deconvoluted peak (Peak #1) observed at ~395 ± 5 nm (3.14 ± 0.04 eV) is mainly due to the recombination of excitonic band [61,62]. Similarly, excitonic energy values of ZnO structures were reported to vary between 3.12 and 3.26 eV [13,61–64].

A violet/blue emission peak at about 420 nm (2.95 eV), two blue emission peaks at ~442 nm (2.81 eV) and ~485 nm (2.56 eV) and a green emission peak nearby 523 nm (2.37 eV) are also identified with a few to several nm shifts in the PL spectra of the ZnO samples. These violet/blue and blue emission centers are related to Zn defects. Zeng et al. (2010) proposed that blue emissions centered at 415, 440, 455 and 488 nm are due to transitions of Zn interstitials (Zn_i) based on the results of EPR spectroscopy [65]. Blue emissions were also observed in the PL spectra of the other ZnO samples. For example, PL spectra of nanoparticles, nanosheets and nanoflowers indicated three common blue emission peaks at about 420 nm (2.95 eV), 456 nm (2.71 eV) and 484 nm (2.56 eV) [61]. In another study, PL spectrum of ZnO nanosheets was deconvoluted into two blue emission peaks at 424 nm (2.92 eV) and 451 nm (2.75 eV) [62].

The Peak #2 (~2.95 eV) in Table 2, can be assigned to the Zn_i to VB transitions, in consistent with the calculated (2.9 eV above VB) and experimentally determined (0.22 eV below CB) energy levels of Zn_i, [61,65]. It was also proposed that electrons at CB or Zn_i state can further relax to extended Zn_i states and, then, they finally can reach VB with blue emissions. The position of extended Zn_i states is slightly below Zn_i state [62,65]. Therefore, the Peak #3 (2.81 eV), can be attributed to the transitions from extended Zn_i state to VB. Considering the position of zinc vacancies (V_{Zn}), which is 0.30 eV above VB, the Peak #3, can also be due to Zn_i to V_{Zn} transitions. Transitions from

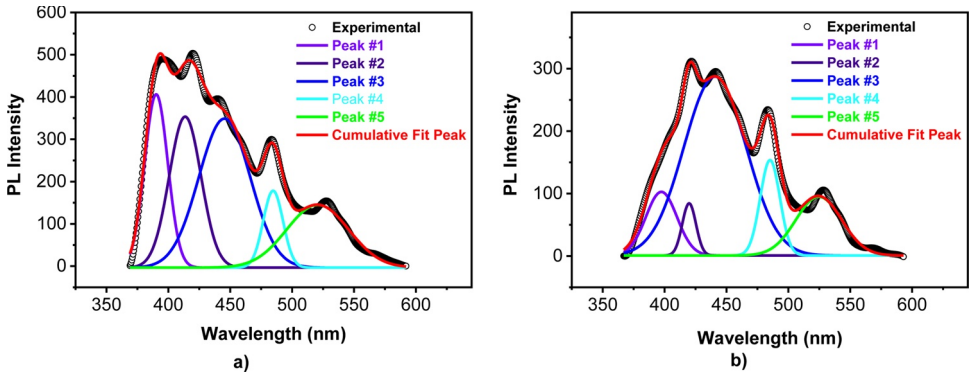

Fig. 6. Deconvoluted PL spectra of a) CZ-0.5-700, b) CZ-1-700.

Table 2
Summary of deconvolution results of PL spectra of ZnO samples.

Sample	Peak #1 3.94 ± 0.04 eV		Peak #2 2.97 ± 0.02 eV		Peak #3 2.80 ± 0.02 eV		Peak #4 2.56 eV		Peak #5 2.37 ± 0.01 eV	
	Value (nm)	Area (%)	Value (nm)	Area (%)	Value (nm)	Area (%)	Value (nm)	Area (%)	Value (nm)	Area (%)
CZ-0 − 700	399	11	420	4	441	58	485	9	523	18
CZ-0.1 − 350	394	16	419	4	442	51	485	10	525	19
CZ-0.1 − 700	400	9	420	4	442	53	485	8	521	26
CZ-0.5 − 700	390	18	414	22	445	35	485	7	521	18
CZ-1 − 700	397	11	420	4	441	60	485	10	525	15
CZ-1.5 − 700	400	14	419	7	440	57	485	10	525	11
Possible assignments	FX → VB		Zn_i → VB		ex-Zn_i → VB Zn_i → V_{Zn}		ex-Zn_i → V_{Zn}		CB → O_{Zn} $\cdot O_2^-$ → VB	

extended Zn_i states to V_{Zn} are also possible. Thus, Peak #4 at 485 nm (2.56 eV) is likely to correspond to extended Zn_i state to V_{Zn} transitions [61,62].

Green emission in PL spectra of all samples is centered at 523 ± 2 nm (2.37 ± 0.01 eV), very close to the reported value (520 nm = 2.38 eV) of green emission center of ZnO films [66], nanorods [67], and nanowires [68]. In order to identify the nature of defects associated with 520 nm peak, these film, nanorod, and nanowire samples were annealed under different atmospheres. More specifically, reducing conditions at high temperatures were used to introduce oxygen vacancies (V_O) and Zn_i into ZnO structures [66,67]. Annealing of ZnO nanorods under 20 % H_2 in Ar atmosphere caused an increase in the peak intensity at 520 nm whereas annealing under oxygen flow at the same temperature and time interval did not change the peak intensity significantly [67]. Similarly, stronger peak signal at 520 nm was observed upon vacuum annealing after oxidation of the nanowires [68]. Thus, the green emission at 520 nm was attributed to V_O [68] or both V_O and Zn_i defects [67]. Conversely, the opposite behavior was observed in another study. For ZnO films, intensity of the green emission enhanced as partial pressure of oxygen in the annealing atmosphere increased at constant annealing temperature. Additionally, at the same annealing atmosphere, intensity of the green emission also enhanced as temperature increased. Hence, V_{Zn}, oxygen interstitial (O_i) and antisite oxygen (O_{Zn}) defects were suggested to be generated by annealing under oxidizing conditions and high temperatures. Considering the calculated energy levels of V_{Zn}, O_i and O_{Zn}, reported as 3.06 eV, 2.28 eV and 2.38 eV below CB, green emission at 520 nm was attributed to O_{Zn} defects [66]. In another study, the green emission observed at 2.25 eV was shown to be due to the surface superoxide ($\cdot O_2^-$) formation, rather than surface hydroxylation or native defects such as V_O based on the conductivity and PL measurements of ZnO nanoparticle films taken under various atmospheric conditions [69].

Comparison of the areas of the green emission peaks of CZ-0.1 − 350 and CZ-0.1 − 700 at 520 nm given in Table 2 indicates that % area of this peak increases as calcination temperature increases. Because calcination under oxygen containing atmosphere at the higher temperature is expected to fix oxygen vacancy defects, antisite oxygen defects or surface superoxide formation is likely to contribute to the green emission associated with Peak #5.

Room temperature PL spectra of the other samples, CZ-0.5 − 350, CZ-1 − 350, and CZ-1.5 − 350 are given in Fig. S8. PL signals of these samples are weaker than those of the ZnO samples. The sample with unidentified crystal structure, CZ-0.5 − 350, has slightly different PL pattern compared to the PL spectra of the ZnS samples, CZ-1 − 350, and CZ-1.5 − 350. However, four peaks with small shifts are apparent in all samples. The first peak at about 330 nm (3.75 eV) is due to excitonic emissions and this value is very close to the excitonic transition energy of ZnS nanowires reported as ~3.68 eV [70]. The second peak observed at ~420 nm (2.95 eV) can be related to interstitial defects [71]. Denzler et al. (1998) suggested that because of the larger size of sulfur, position of sulfur interstitial (S_i) defects should be blue-shifted relative to that of Zn_i. By simple deconvolution of the spectrum, the authors determined the positions of S_i and Zn_i bands as 416 nm and 424 nm, respectively [72]. For CZ-1.5 − 350, the peak position of interstitial defects is 3 nm blue-shifted compared to those of CZ-0.5 − 350 and CZ-1 − 350 suggesting the presence of higher amount of S_i in CZ-1.5 − 350. Because initial cysteine content of CZ-1.5 − 350 is higher than those of the others, CZ-1.5 − 350 is likely to have more S_i defects corroborating with the suggested positions of interstitial defects. For the ZnS samples, another blue emission at 456 nm (2.72 eV) was also obtained. This peak is a few nm blue-shifted for CZ-0.5 − 350. McClean and Thomas (1992) also observed a peak around 460 nm for ZnS films. Annealing of the films at 400 °C under N_2 atmosphere increased the peak intensity upon release of sulfur suggesting that the blue emission was related to sulfur vacancy. The authors also observed that the peak intensity decreased upon controlled reduction of zinc vacancies and proposed that the blue emission was due to S-Zn vacancies acting as self-activated centers [73]. Thus, the third peak observed at 456 nm can be attributed to sulfur and zinc vacancies. Finally, the last peak observed at about 490 nm (2.53 eV) can also be due to zinc vacancies [74].

3.4. XPS and EPR spectroscopy results

XPS and EPR measurements were also performed to analyze the crystal defects of select ZnO samples. XPS survey scans of the samples, CZ-0 − 700, CZ-0.5 − 700, and CZ-1 − 700 are given in Fig. S9. XPS spectra indicate Zn 2s, Zn 2p, Zn 3s, Zn 3p, Zn 3d, Zn LMM, O 1s, and O KLL peaks confirming high purity of the samples [75–77]. To provide further evidence for Zn_i defects indicated by PL spectra, Auger Zn $L_3M_{4.5}M_{4.5}$ peaks of the samples observed with a maximum of 498.5 ± 0.5 eV were used (Fig. 7). Deconvolution of this peak yielded two peaks centered at 495.3 ± 0.5 eV and 498.5 ± 0.5 eV. The high binding energy peak is due to the lattice Zn^{2+} whereas the shoulder peak with low binding energy reveals the presence of the metallic Zn, in other words, Zn_i defects [78–81]. Auger Zn $L_3M_{4.5}M_{4.5}$ peaks also indicate that Zn_i peak areas of CZ-0.5 − 700, and CZ-1 − 700 are close to each other and are slightly higher than that of CZ-0 − 700.

EPR spectra of the samples CZ-0 − 700, CZ-0.5 − 700, and CZ-1 − 700 are given in Fig. 8. For all samples an EPR signal at about g = 2.01 was observed. CZ-0 − 700 has the strongest signal whereas a quite weak signal was obtained for CZ-1 − 700. The EPR signal at g ≈ 2.0 was mostly proposed to be due to singly charged vacancies (V_O^+ or V_{Zn}^-) [82,83]. However, g ≈ 2.0 signal was also attributed to surface defects based on the core shell model and this signal was shown to be correlated with the red emissions in PL data, originated from V_O^+ [84].

3.5. Rhodamine B photodegradation activities

RhB removal profiles of the samples calcined at 350 °C and at 700 °C are given in Fig. S10 and Fig. 9a, respectively. All the samples calcined at 700 °C exhibited UV-light induced dye photodegradation activity. The samples calcined at 350 °C, on the other hand, removed the dye mostly by adsorption rather than photodegradation.

At low dye concentrations, the number of catalytic sites is not the

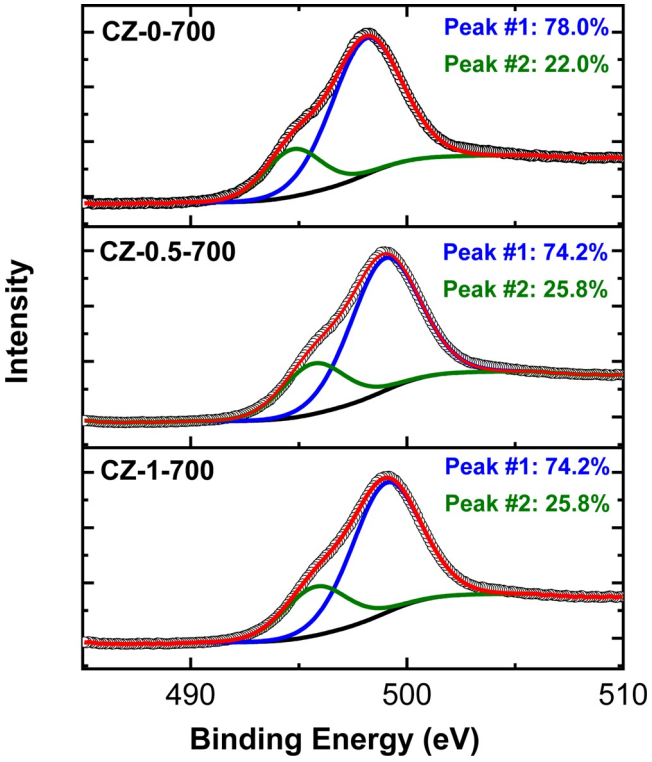

Fig. 7. Auger Zn $L_3M_{4.5}M_{4.5}$ spectra of CZ-0-700, CZ-0.5-700, and CZ-1-700.

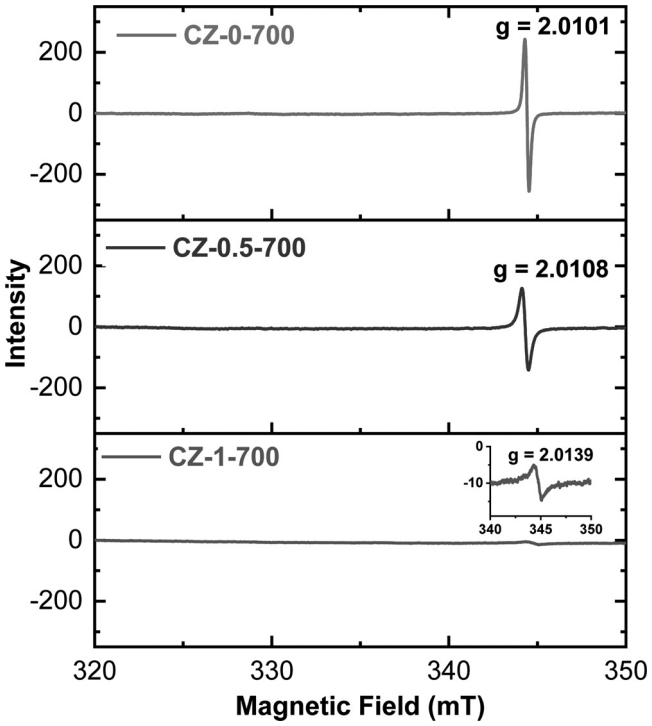

Fig. 8. EPR spectra of CZ-0-700, CZ-0.5-700, and CZ-1-700.

limiting factor and photodegradation rate is proportional to the dye concentration. Thus, the reaction kinetics can be described by the apparent first order kinetics as follows [85]:

$$\frac{dC}{dt} = kC \tag{4}$$

where k is the rate constant. Integrated form of the equation is:

$$\ln\frac{C_o}{C} = kt \tag{5}$$

Photodegradation first-order kinetic plots of the samples calcined at 700 °C are given in Fig. 9b. Calculated rate constants and R^2 values are summarized in Table 3. Linear lines obtained in the kinetic plots confirm that the photodegradation process follows the apparent first-order reaction kinetics. The sample CZ-0.5−700 exhibited the fastest RhB degradation kinetics whereas the slowest degradation rate was observed for the sample prepared in the absence of L-cysteine, CZ-0−700. The other samples, CZ-0.1−700, CZ-1−700, and CZ-1.5−700 showed similar photodegradation activities.

Photocatalytic activity of the semiconductors can be dictated by many factors including band gap, morphology, surface area, and defects. UV spectra given in Fig. 5 indicate that positions of the excitonic peak and, hence, band gap energy values of the ZnO samples are close to each other. SEM pictures show that CZ-0.5−700, CZ-1−700 and CZ-1.5−700 have all spherical morphology (Fig. 4 and Fig. S5). Among these three samples, CZ-0.5−700 has the highest surface area because of its lower size. Surface area of CZ-0.1−350 is higher than those of the samples calcined at 700 °C but its photocatalytic performance is quite low most probably because of some organic residuals in this sample (Fig. S4a).

Photocatalytic activity of the samples can also be governed by their crystal defects because some differences in the PL spectra of the samples were observed. Indeed, contributions of V_O defects to the photodegradation activities of ZnO catalysts were reported [13,14,18,86]. Besides, Zn_i defects can also promote photocatalytic degradation process, even though Zn_i defects were proposed to accelerate photocatalytic activity less efficiently than V_O [13].

XPS analyses show that the samples, CZ-0−700, CZ-0.5−700 and CZ-1−700 have similar Zn_i contents. However, deconvolution of the purple/blue emission region of the PL spectra of the ZnO samples yielded three peaks associated with different forms of Zn_i transitions. One striking difference is that % area of Peak #2 in PL spectrum of CZ-0.5−700 (the sample with the highest photocatalytic activity) is much higher than those of the other ZnO samples (Table 2). Peak #2 corresponds to the transition of neutral Zn_i to the VB whereas the others (Peak #3 and Peak #4) are mostly related to extended states of Zn_i that form as a result of ionization reactions. For titania photocatalysts, Ohtani (2013) proposed that shallow traps can enhance photocatalytic activity by facilitating the migration of electrons through CB and traps. The author also suggested that deep traps may reduce photocatalytic activity as a result of higher probability of electron-hole recombination. Thus, shallow donors can participate the electron transport processes by donating electrons to CB with the formation of electron deficient levels (electron traps) and, then, by accepting photoexcited electrons to these traps [87]. Energy state of neutral Zn_i defects (shallow donors) is closer to the CB compared to those of the ionized forms of Zn_i and, hence, neutral Zn_i defects are more likely to participate charge separation process. Additionally, high surface area of CZ-0.5−700 can also contribute to superior photocatalytic activity of this sample by providing more active sites for the reaction and by facilitating the diffusion of the reactants during the photodegradation reaction [88].

Two main routes, direct and indirect oxidation, were proposed for the photodegradation of dyes by semiconductors. In the direct oxidation, the degradation occurs because of charge transfer between dye and photogenerated carriers such as holes and electrons that form immediately via irradiation of the semiconductor. Reactive oxygen species such as OH radicals (OH·) and superoxide radicals ($\cdot O_2^-$) generated as a result of adsorption of hydroxyl, water or molecular oxygen dissolved in water on the semiconductor surface can also mediate photodegradation process by indirect oxidation [89,90]. Among these different mechanisms, OH· accelerated photodegradation was regarded to dominate most of the dye photodegradation processes [48,89–94]. In the case of RhB photodegradation, OH· was reported to rupture the cyclic structure of

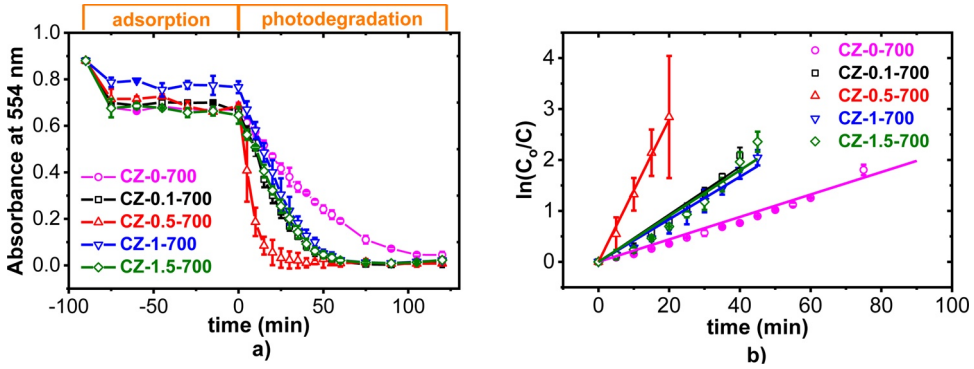

Fig. 9. a) Rhodamine B removal profiles and b) photodegradation first-order kinetic plots of the samples calcined at 700 °C.

Table 3
Photodegradation kinetic parameters of the samples calcined at 700 °C.

Sample	k (min^{-1})	R^2
CZ-0 – 700	0.022 ± 0.001	0.988
CZ-0.1 – 700	0.047 ± 0.002	0.987
CZ-0.5 – 700	0.140 ± 0.003	0.998
CZ-1 – 700	0.042 ± 0.002	0.988
CZ-1.5 – 700	0.045 ± 0.002	0.976

the dye and to induce total mineralization [94]. Generation of OH· radicals by the holes depends on the potential value of the VB. If the valence band edge position (E_{VB}) of the semiconductor is more positive than the redox potential value of OH·/H_2O, formation of OH· radicals is thermodynamically feasible [95]. The valence band edge position (E_{VB}) and the conduction band edge position (E_{CB}) of the semiconductors can be calculated using the following equations based on the Mulliken electronegativity theory:

$$E_{VB}[eV\ vs.\ NHE] = \chi - 4.5 + \frac{E_g}{2} \quad (6)$$

$$E_{CB}[eV\ vs.\ NHE] = E_{VB} - E_g \quad (7)$$

where χ is the absolute electronegativity and E_g is the band gap energy [96,97]. Optical band gap energies of the representative ZnO and ZnS samples were estimated using $\lambda_{1/2}$ method by taking $\lambda_{1/2}$ as the wavelength, at which the absorption is 50 % of that at the excitonic peak [98]. E_g values (in eV) were, then, calculated by applying the simple formula, $E_g = 1240/\lambda_{1/2}$, where $\lambda_{1/2}$ is in nm. The parameters used in these equations and calculated E_{VB} and E_{CB} values of the representative ZnO and ZnS samples are given in Table S1. E_{VB} values of ZnO and ZnS were estimated as 2.89 eV vs. NHE and 2.55 eV vs. NHE, respectively. Calculated E_{VB} values are greater than OH·/H_2O potential value reported as ~2.3 ± 0.1 eV vs. NHE indicating that both ZnO and ZnS semiconductors synthesized in the current study are capable of generating OH· radicals [95,99,100]. E_{CB} values determined as -0.31 eV vs. NHE and -1.03 eV vs. NHE for ZnO and ZnS, respectively are more negative than potential value of O_2/·O_2^-, -0.28 eV vs. NHE [100,101]. These results indicate that thermodynamically, photogenerated ZnO holes have a higher oxidation potential to form hydroxyl radical species compared to the ZnS holes. In addition to this, excited ZnO electrons have a much lower reduction potential than excited ZnS electrons to catalyze reduction of dioxygen species to superoxide anions. We observed that only ZnO samples have photodegradation ability and that ZnS removes the dye by adsorption. Thus, RhB photodegradation is mainly dictated by the extent of the oxidation reactions initiated in the valence band.

To test the correlation between OH· generation and photocatalytic activity, we compared relative amounts of OH· formed on select ZnO sample surfaces by using TPA as a probe molecule. For CZ-0 – 700 (control sample), CZ-0.1 – 350 (the sample with the highest surface area) and CZ-0.5 – 700 and CZ-1 – 700 (the samples mainly focused in the current study), PL signals of HTA evolved as a result of the reaction between OH· and TPA are given in Fig. 10. CZ-0.1 – 350, which removed RhB by adsorption predominantly, generated negligible amount of OH· radicals. The sample with the highest RhB photodegradation activity, CZ-0.5 – 700, released the highest amount of OH· at the early stages of the irradiation exposure. The kinetics of OH· formation of the other two samples is slower compared to that of CZ-0.5 – 700. These observations indicate that charge separation is more efficient for CZ-0.5 – 700 and that RhB photodegradation mechanism of the samples is mainly by indirect oxidation.

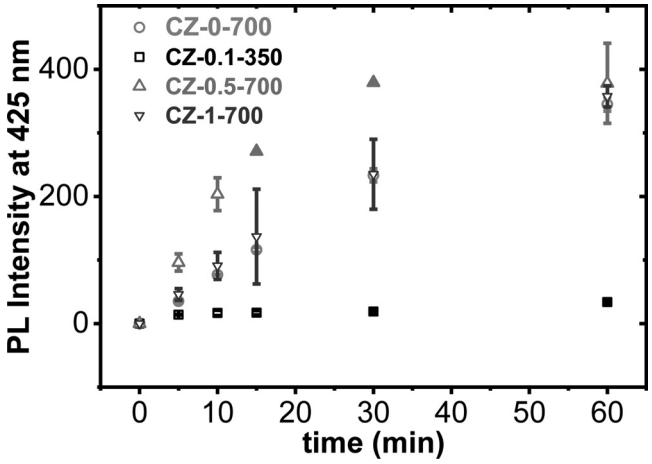

Fig. 10. OH· radical generation kinetics of select samples.

4. Conclusions

L-cysteine was used as an additive in the synthesis of the precursors that form as a result of aqueous precipitation reaction of $Zn(NO_3)_2$ and NaOH. ZnO and ZnS structures were obtained by simply using certain Cys:Zn ratios in the preparation of the precursors and by calcining these precursors at specific temperatures. A variety of morphologies including spherical nanoparticles, plate-like, cauliflower-like and interconnected structures were observed in the SEM pictures of the samples obtained.

Blue and green emission centers with similar peak positions were detected in the PL spectra of the samples. However, different peak areas obtained in the deconvolution of the PL spectra indicate that defect densities of the samples are different. Among all samples, the highest photodegradation activity was exhibited by the sample CZ-0.5 – 700, which has above average surface area and has the highest peak area associated with neutral Zn_i to VB transitions observed at ~420 nm in its PL spectrum. The samples calcined at 350 °C removed the dye mainly

by adsorption process.

In conclusion, we showed that chemical composition, morphology, surface area and defect properties of the semiconductor photocatalysts can easily be tuned by changing the concentration of the additive and by applying different calcination temperatures. We also demonstrated that these simple synthesis route modifications can provide opportunities to increase the performance of semiconductor photocatalysts.

Declaration of Competing Interest

The authors declare that they have no known competing financial interests or personal relationships that could have appeared to influence the work reported in this paper.

Acknowledgements

We thank to Materials Research Center at Izmir Institute of Technology for XRD and SEM experiments. Biotechnology and Bioengineering Research and Application Center at İzmir Institute of Technology is acknowledged for making UV–vis spectroscopy measurements possible. We also thank to Dr. Yaşar Akdoğan for kindly performing the EPR experiments.

Appendix A. Supplementary data

Supplementary material related to this article can be found, in the online version, at doi:https://doi.org/10.1016/j.mtcomm.2020.101573.

References

[1] N.S. Alharbi, B. Hu, T. Hayat, S.O. Rabah, A. Alsaedi, L. Zhuang, X. Wang, Efficient elimination of environmental pollutants through sorption-reduction and photocatalytic degradation using nanomaterials, Front. Chem. Sci. Eng. (2020), https://doi.org/10.1007/s11705-020-1923-z.

[2] R. Gusain, K. Gupta, P. Joshi, O.P. Khatri, Adsorptive removal and photocatalytic degradation of organic pollutants using metal oxides and their composites: a comprehensive review, Adv. Colloid Interface Sci. 272 (2019) 102009,, , https://doi.org/10.1016/j.cis.2019.102009.

[3] H. Zangeneh, A. Zinatizadeh, M. Habibi, M. Akia, M.H. Isa, Photocatalytic oxidation of organic dyes and pollutants in wastewater using different modified titanium dioxides: a comparative review, J. Ind. Eng. Chem. 26 (2015) 1–36, https://doi.org/10.1016/j.jiec.2014.10.043.

[4] W.S. Koe, J.W. Lee, W.C. Chong, Y.L. Pang, L.C. Sim, An overview of photocatalytic degradation: photocatalysts, mechanisms, and development of photocatalytic membrane, Environ. Sci. Pollut. Res. 27 (2020) 2522–2565, https://doi.org/10.1007/s11356-019-07193-5.

[5] A. Buthiyappan, A.R.A. Aziz, W.M.A.W. Daud, Recent advances and prospects of catalytic advanced oxidation process in treating textile effluents, Rev. Chem. Eng. 32 (2016) 1–47, https://doi.org/10.1515/revce-2015-0034.

[6] M. Karimi-Shamsabadi, A. Nezamzadeh-Ejhieh, Comparative study on the increased photoactivity of coupled and supported manganese-silver oxides onto a natural zeolite nano-particles, J. Mol. Catal. A Chem. 418 (2016) 103–114, https://doi.org/10.1016/j.molcata.2016.03.034.

[7] A.G. Akerdi, S.H. Bahrami, Application of heterogeneous nano-semiconductors for photocatalytic advanced oxidation of organic compounds: a review, J. Environ. Chem. Eng. 7 (2019) 103283, , https://doi.org/10.1016/j.jece.2019.103283.

[8] C.B. Ong, L.Y. Ng, A.W. Mohammad, A review of ZnO nanoparticles as solar photocatalysts: synthesis, mechanisms and applications, Renew. Sust. Energ. Rev. 81 (2018) 536–551, https://doi.org/10.1016/j.rser.2017.08.020.

[9] B. Bethi, S.H. Sonawane, B.A. Bhanvase, S.P. Gumfekar, Nanomaterials-based advanced oxidation processes for wastewater treatment: a review, Chem. Eng. Process. 109 (2016) 178–189, https://doi.org/10.1016/j.cep.2016.08.016.

[10] D. Doğu, G. Karakaş, Methylene blue degradation on praseodymium-doped titanium dioxide photocatalyst, J. Fac. Eng. Archit. Gazi Univ 35 (2020) 859–870, https://doi.org/10.17341/gazimmfd.549084.

[11] A. Pourtaheri, A. Nezamzadeh-Ejhieh, Enhancement in photocatalytic activity of NiO by supporting onto an Iranian clinoptilolite nano-particles of aqueous solution of cefuroxime pharmaceutical capsule, Spectrochim. Acta A. Mol. Biomol. Spectrosc. 137 (2015) 338–344, https://doi.org/10.1016/j.saa.2014.08.058.

[12] M.D. Hernández-Alonso, F. Fresno, S. Suárez, J.M. Coronado, Development of alternative photocatalysts to TiO_2: challenges and opportunities, Energy Environ. Sci. 2 (2009) 1231–1257, https://doi.org/10.1039/B907933E.

[13] F. Kayaci, S. Vempati, I. Donmez, N. Biyikli, T. Uyar, Role of zinc interstitials and oxygen vacancies of ZnO in photocatalysis: a bottom-up approach to control defect density, Nanoscale 6 (2014) 10224–10234, https://doi.org/10.1039/C4NR01887G.

[14] Y. Zheng, C. Chen, Y. Zhan, X. Lin, Q. Zheng, K. Wei, J. Zhu, Y. Zhu, Luminescence and photocatalytic activity of ZnO nanocrystals: correlation between structure and property, Inorg. Chem. 46 (2007) 6675–6682, https://doi.org/10.1021/ic062394m.

[15] D. Chen, Z. Wang, T. Ren, H. Ding, W. Yao, R. Zong, Y. Zhu, Influence of defects on the photocatalytic activity of ZnO, J. Phys. Chem. C. 118 (2014) 15300–15307, https://doi.org/10.1021/jp5033349.

[16] A. Kajbafvala, H. Ghorbani, A. Paravar, J.P. Samberg, E. Kajbafvala, S. Sadrnezhaad, Effects of morphology on photocatalytic performance of zinc oxide nanostructures synthesized by rapid microwave irradiation methods, Superlattices Microstruct. 51 (2012) 512–522, https://doi.org/10.1016/j.spmi.2012.01.015.

[17] T.A. Kusumam, T. Panakkal, T. Divya, M. Nikhila, M. Anju, K. Anas, N. Renuka, Morphology controlled synthesis and photocatalytic activity of zinc oxide nanostructures, Ceram. Int. 42 (2016) 3769–3775, https://doi.org/10.1016/j.ceramint.2015.11.025.

[18] X. Zhang, J. Qin, Y. Xue, P. Yu, B. Zhang, L. Wang, R. Liu, Effect of aspect ratio and surface defects on the photocatalytic activity of ZnO nanorods, Sci. Rep. 4 (2014) 4596, https://doi.org/10.1038/srep04596.

[19] M.M. Khin, A.S. Nair, V.J. Babu, R. Murugan, S. Ramakrishna, A review on nanomaterials for environmental remediation, Energy Environ. Sci. 5 (2012) 8075–8109, https://doi.org/10.1039/C2EE21818F.

[20] T. Jiang, Y. Wang, D. Meng, X. Wu, J. Wang, J. Chen, Controllable fabrication of CuO nanostructure by hydrothermal method and its properties, Appl. Surf. Sci. 311 (2014) 602–608, https://doi.org/10.1016/j.apsusc.2014.05.116.

[21] A. Janotti, C.G. Van de Walle, Fundamentals of zinc oxide as a semiconductor, Rep. Prog. Phys. 72 (2009) 126501, , https://doi.org/10.1088/0034-4885/72/12/126501.

[22] A.B. Djurišić, A.M.C. Ng, X.Y. Chen, ZnO nanostructures for optoelectronics: material properties and device applications, Prog. Quant. Electron. 34 (2010) 191–259, https://doi.org/10.1016/j.pquantelec.2010.04.001.

[23] M. Godlewski, E. Guziewicz, K. Kopalko, G. Łuka, M. Łukasiewicz, T. Krajewski, B. Witkowski, S. Gierałtowska, Zinc oxide for electronic, photovoltaic and optoelectronic applications, Low Temp. Phys. 37 (2011) 235–240, https://doi.org/10.1063/1.3570930.

[24] X. Wang, H. Huang, B. Liang, Z. Liu, D. Chen, G. Shen, ZnS nanostructures: synthesis, properties, and applications, Crit. Rev. Solid State 38 (2013) 57–90, https://doi.org/10.1080/10408436.2012.736887.

[25] P. D'Amico, A. Calzolari, A. Ruini, A. Catellani, New energy with ZnS: novel applications for a standard transparent compound, Sci. Rep. 7 (2017) 16805, https://doi.org/10.1038/s41598-017-17156-w.

[26] J. Theerthagiri, S. Salla, R. Senthil, P. Nithyadharseni, A. Madankumar, P. Arunachalam, T. Maiyalagan, H.S. Kim, A review on ZnO nanostructured materials: energy, environmental and biological applications, Nanotechnology 30 (2019) 392001, , https://doi.org/10.1088/1361-6528/ab268a.

[27] K. Rajeshwar, M. Osugi, W. Chanmanee, C. Chenthamarakshan, M.V.B. Zanoni, P. Kajitvichyanukul, R. Krishnan-Ayer, Heterogeneous photocatalytic treatment of organic dyes in air and aqueous media, J. Photochem. Photobiol. C: Photochem. Rev. 9 (2008) 171–192, https://doi.org/10.1016/j.jphotochemrev.2008.09.001.

[28] H. Zhang, G. Chen, D.W. Bahnemann, Photoelectrocatalytic materials for environmental applications, J. Mater. Chem. 19 (2009) 5089–5121, https://doi.org/10.1039/B821991E.

[29] D. Neena, K.K. Kondamareddy, H. Bin, D. Lu, P. Kumar, R. Dwivedi, V.O. Pelenovich, X.Z. Zhao, W. Gao, D. Fu, Enhanced visible light photodegradation activity of RhB/MB from aqueous solution using nanosized novel Fe-Cd co-modified ZnO, Sci. Rep. 8 (2018) 10691, , https://doi.org/10.1038/s41598-018-29025-1.

[30] W. Raza, S.M. Faisal, M. Owais, D. Bahnemann, M. Muneer, Facile fabrication of highly efficient modified ZnO photocatalyst with enhanced photocatalytic, antibacterial and anticancer activity, RSC Adv. 6 (2016) 78335–78350, https://doi.org/10.1039/C6RA06774C.

[31] G. Wang, B. Huang, Z. Li, Z. Lou, Z. Wang, Y. Dai, M.H. Whangbo, Synthesis and characterization of ZnS with controlled amount of S vacancies for photocatalytic H_2 production under visible light, Sci. Rep. 5 (2015) 8544, https://doi.org/10.1038/srep08544.

[32] F. Kurnia, Y.H. Ng, R. Amal, N. Valanoor, J.N. Hart, Defect engineering of ZnS thin films for photoelectrochemical water-splitting under visible light, Sol. Energy Mater. Sol. Cells 153 (2016) 179–185, https://doi.org/10.1016/j.solmat.2016.04.021.

[33] X. Hao, Y. Wang, J. Zhou, Z. Cui, Y. Wang, Z. Zou, Zinc vacancy-promoted photocatalytic activity and photostability of ZnS for efficient visible-light-driven hydrogen evolution, Appl. Catal. B 221 (2018) 302–311, https://doi.org/10.1016/j.apcatb.2017.09.006.

[34] L. Tie, R. Sun, H. Jiang, Y. Liu, Y. Xia, Y.Y. Li, H. Chen, C. Yu, S. Dong, J. Sun, Facile fabrication of N-doped ZnS nanomaterials for efficient photocatalytic performance of organic pollutant removal and H_2 production, J. Alloys. Compd. 807 (2019) 151670, , https://doi.org/10.1016/j.jallcom.2019.151670.

[35] Y. Li, W. Xie, X. Hu, G. Shen, X. Zhou, Y. Xiang, X. Zhao, P. Fang, Comparison of dye photodegradation and its coupling with light-to-electricity conversion over TiO_2 and ZnO, Langmuir 26 (2009) 591–597, https://doi.org/10.1021/la902117c.

[36] C. Tian, Q. Zhang, A. Wu, M. Jiang, Z. Liang, B. Jiang, H. Fu, Cost-effective large-scale synthesis of ZnO photocatalyst with excellent performance for dye photodegradation, Chem. Commun. (Camb.) 48 (2012) 2858–2860, https://doi.org/10.1039/C2CC16434E.

[37] M.T. Thein, S.Y. Pung, L.S. Chuah, Y.F. Pung, Photodegradation behavior of ZnO

nanorods on various types of organic dyes, Adv. Mater. Process. Technol. 4 (2018) 272–280, https://doi.org/10.1080/2374068X.2017.1416882.
[38] L. Daneshvar, A. Nezamzadeh-Ejhieh, Photocatalytic activity of ZnO nanoparticles towards tinidazole degradation: experimental design by response surface methodology (RSM), Desalin. Water Treat. 141 (2019) 364–376, https://doi.org/10.5004/dwt.2019.23310.
[39] W. Vallejo, A. Cantillo, C. Díaz-Uribe, Methylene blue photodegradation under visible irradiation on Ag-doped ZnO thin films, Int. J. Photoenergy 2020 (2020) 1627498, , https://doi.org/10.1155/2020/1627498.
[40] J. Esmaili-Hafshejani, A. Nezamzadeh-Ejhieh, Increased photocatalytic activity of Zn (II)/Cu (II) oxides and sulfides by coupling and supporting them onto clinoptilolite nanoparticles in the degradation of benzophenone aqueous solution, J. Hazard. Mater. 316 (2016) 194–203, https://doi.org/10.1016/j.jhazmat.2016.05.006.
[41] J.E. Rodríguez-Paéz, A.C. Caballero, M. Villegas, C. Moure, P. Durán, J.F. Fernández, Controlled precipitation methods: formation mechanism of ZnO nanoparticles, J. Eur. Ceram. Soc. 21 (2001) 925–930, https://doi.org/10.1016/S0955-2219(00)00283-1.
[42] J.J. Macías-Sánchez, L. Hinojosa-Reyes, A. Caballero-Quintero, W. de la Cruz, E. Ruiz-Ruiz, A. Hernández-Ramírez, J.L. Guzmán-Mar, Synthesis of nitrogen-doped ZnO by sol–gel method: characterization and its application on visible photocatalytic degradation of 2,4-D and picloram herbicides, Photochem. Photobiol. Sci. 14 (2015) 536–542, https://doi.org/10.1039/C4PP00273C.
[43] Z. Zarghami, M. Ramezani, K. Motevalli, ZnO nanorods/nanoparticles: novel hydrothermal synthesis, characterization and formation mechanism for increasing the efficiency of dye-sensitized solar cells, J. Cluster Sci. 27 (2016) 1451–1462, https://doi.org/10.1007/s10876-016-1011-1.
[44] W. Feng, P. Huang, B. Wang, C. Wang, W. Wang, T. Wang, S. Chen, R. Lv, Y. Qin, J. Ma, Solvothermal synthesis of ZnO with different morphologies in dimethylacetamide media, Ceram. Int. 42 (2016) 2250–2256, https://doi.org/10.1016/j.ceramint.2015.10.018.
[45] V. Svetlichnyi, A. Shabalina, I. Lapin, D. Goncharova, A. Nemoykina, ZnO nanoparticles obtained by pulsed laser ablation and their composite with cotton fabric: preparation and study of antibacterial activity, Appl. Surf. Sci. 372 (2016) 20–29, https://doi.org/10.1016/j.apsusc.2016.03.043.
[46] A.J. Cheng, Y. Tzeng, Y. Zhou, M. Park, T.H. Wu, C. Shannon, D. Wang, W. Lee, Thermal chemical vapor deposition growth of zinc oxide nanostructures for dye-sensitized solar cell fabrication, Appl. Phys. Lett. 92 (2008) 092113, , https://doi.org/10.1063/1.2889502.
[47] J.M. Wu, T.W. Zhang, Photodegradation of rhodamine B in water assisted by titania films prepared through a novel procedureJ, Photochem. Photobiol. A Chem. 162 (2004) 171–177, https://doi.org/10.1016/S1010-6030(03)00345-9.
[48] S.M. Lam, J.C. Sin, A.Z. Abdullah, A.R. Mohamed, Investigation on visible-light photocatalytic degradation of 2,4-dichlorophenoxyacetic acid in the presence of MoO_3/ZnO nanorod composites, J. Mol. Catal. A Chem. 370 (2013) 123–131, https://doi.org/10.1016/j.molcata.2013.01.005.
[49] A. Top, H. Çetinkaya, Zinc oxide and zinc hydroxide formation via aqueous precipitation: effect of the preparation route and lysozyme addition, Mater. Chem. Phys. 167 (2015) 77–87, https://doi.org/10.1016/j.matchemphys.2015.10.013.
[50] H. Ma, X. Cheng, C. Ma, X. Dong, X. Zhang, M. Xue, X. Zhang, Y. Fu, Synthesis, characterization, and photocatalytic activity of N-doped ZnO/ZnS composites, Int. J. Photoenergy 2013 (2013) 625024, , https://doi.org/10.1155/2013/625024.
[51] N. Gonçalves, J. Carvalho, Z. Lima, J. Sasaki, Size–strain study of NiO nanoparticles by X-ray powder diffraction line broadening, Mater. Lett. 72 (2012) 36–38, https://doi.org/10.1016/j.matlet.2011.12.046.
[52] N. Omrania, A. Nezamzadeh-Ejhieha, M. Alizadehb, Brief study on the kinetic aspect of photodegradation of sulfasalazine aqueous solution by cuprous oxide/cadmium sulfide nanoparticles, Desalin. Water Treat. 162 (2019) 290–302, https://doi.org/10.5004/dwt.2019.24352.
[53] A. Ramadani, S. Pratapa, Line broadening correction in X-ray diffraction analysis for nanomaterials characterization using calcined yttrium oxide powder as a standard material, Proceeding of International Conference on Research, Implementation and Education of Mathematics and Sciences, Yogyakarta State University 17–19 (2015) 17–19 May available at https://eprints.uny.ac.id/21034/.
[54] F. Kogelheide, K. Kartaschew, M. Strack, S. Baldus, N. Metzler-Nolte, M. Havenith, P. Awakowicz, K. Stapelmann, J.W. Lackmann, FTIR spectroscopy of cysteine as a ready-to-use method for the investigation of plasma-induced chemical modifications of macromolecules, J. Phys. D Appl. Phys. 49 (2016) 084004, , https://doi.org/10.1088/0022-3727/49/8/084004.
[55] M.Y. Ghotbi, Synthesis and characterization of nano-sized ε-$Zn(OH)_2$ and its decomposed product, nano-zinc oxide, J. Alloys. Compd. 491 (2010) 420–422, https://doi.org/10.1016/j.jallcom.2009.10.214.
[56] P. Li, Z.P. Xu, M.A. Hampton, D.T. Vu, L. Huang, V. Rudolph, A.V. Nguyen, Control preparation of zinc hydroxide nitrate nanocrystals and examination of the chemical and structural stability, J. Phys. Chem. C 116 (2012) 10325–10332, https://doi.org/10.1021/jp300045u.
[57] V. Stanić, T.H. Etsell, A.C. Pierre, R.J. Mikula, Sol-gel processing of ZnS, Mater. Lett. 31 (1997) 35–38, https://doi.org/10.1016/S0167-577X(96)00237-6.
[58] R. Gärd, Z.X. Sun, W. Forsling, FT-IR and FT-Raman studies of colloidal ZnS: 1. Acidic and alkaline sites at the ZnS/water interface, J. Colloid Interface Sci. 169 (1995) 393–399, https://doi.org/10.1006/jcis.1995.1048.
[59] W. Chen, X. Ran, X. Jiang, H. Min, D. Li, L. Zou, J. Fan, G. Li, Synthesis of TiO_2 and TiO_2-Pt and their application in photocatalytic degradation of humic acid, Water Environ. Res. 86 (2014) 48–55, https://doi.org/10.2175/106143013X13807328848775.
[60] B. Meyer, H. Alves, D. Hofmann, W. Kriegseis, D. Forster, F. Bertram, J. Christen, A. Hoffmann, M. Straßburg, M. Dworzak, Bound exciton and donor–acceptor pair recombinations in ZnO, Phys. Status Solidi B 241 (2004) 231–260, https://doi.org/10.1002/pssb.200301962.
[61] R. Khokhra, B. Bharti, H.N. Lee, R. Kumar, Visible and UV photo-detection in ZnO nanostructured thin films via simple tuning of solution method, Sci. Rep. 7 (2017) 15032, https://doi.org/10.1038/s41598-017-15125-x.
[62] S. Vempati, J. Mitra, P. Dawson, One-step synthesis of ZnO nanosheets: a blue-white fluorophore, Nanoscale Res. Lett. 7 (2012) 470, https://doi.org/10.1186/1556-276X-7-470.
[63] B. Cao, X. Teng, S.H. Heo, Y. Li, S.O. Cho, G. Li, W. Cai, Different ZnO nanostructures fabricated by a seed-layer assisted electrochemical route and their photoluminescence and field emission properties, J. Phys. Chem. C 111 (2007) 2470–2476, https://doi.org/10.1021/jp066661l.
[64] S. Chen, Y. Liu, C. Shao, R. Mu, Y. Lu, J. Zhang, D. Shen, X. Fan, Structural and optical properties of uniform ZnO nanosheets, Adv. Mater. 17 (2005) 586–590, https://doi.org/10.1002/adma.200401263.
[65] H. Zeng, G. Duan, Y. Li, S. Yang, X. Xu, W. Cai, Blue luminescence of ZnO nanoparticles based on non-equilibrium processes: defect origins and emission controls, Adv. Funct. Mater. 20 (2010) 561–572, https://doi.org/10.1002/adfm.200901884.
[66] B. Lin, Z. Fu, Y. Jia, Green luminescent center in undoped zinc oxide films deposited on silicon substrates, Appl. Phys. Lett. 79 (2001) 943–945, https://doi.org/10.1063/1.1394173.
[67] X. Liu, X. Wu, H. Cao, R.P.H. Chang, Growth mechanism and properties of ZnO nanorods synthesized by plasma-enhanced chemical vapor deposition, J. Appl. Phys. 95 (2004) 3141–3147, https://doi.org/10.1063/1.1646440.
[68] D. Banerjee, J.Y. Lao, D.Z. Wang, J.Y. Huang, Z.F. Ren, D. Steeves, B. Kimball, S. M, Large-quantity free-standing ZnO nanowires, Appl. Phys. Lett. 83 (2003) 2061–2063, https://doi.org/10.1063/1.1609036.
[69] J.A. Röhr, J. Sá, S.J. Konezny, The role of adsorbates in the green emission and conductivity of zinc oxide, Commun. Chem. 2 (2019) 52, https://doi.org/10.1038/s42004-019-0153-0.
[70] R. Chen, D. Li, B. Liu, Z. Peng, G.G. Gurzadyan, Q. Xiong, H. Sun, Optical and excitonic properties of crystalline ZnS nanowires: toward efficient ultraviolet emission at room temperature, Nano Lett. 10 (2010) 4956–4961, https://doi.org/10.1021/nl102987z.
[71] W.G. Becker, A.J. Bard, Photoluminescence and photoinduced oxygen adsorption of colloidal zinc sulfide dispersions, J. Phys. Chem. 87 (1983) 4888–4893, https://doi.org/10.1021/j150642a026.
[72] D. Denzler, M. Olschewski, K. Sattler, Luminescence studies of localized gap states in colloidal ZnS nanocrystals, J. Appl. Phys. 84 (1998) 2841–2845, https://doi.org/10.1063/1.368425.
[73] I. McClean, C. Thomas, Photoluminescence study of MBE-grown films on ZnS, Semicond. Sci.Technol. 7 (1992) 1394, https://doi.org/10.1088/0268-1242/7/11/019.
[74] W.T. Yao, S.H. Yu, L. Pan, J. Li, Q.S. Wu, L. Zhang, J. Jiang, Flexible wurtzite-type ZnS nanobelts with quantum-size effects: a diethylenetriamine-assisted solvothermal approach, Small 1 (2005) 320–325, https://doi.org/10.1002/smll.200400079.
[75] R. Al-Gaashani, S. Radiman, A. Daud, N. Tabet, Y. Al-Douri, XPS and optical studies of different morphologies of ZnO nanostructures prepared by microwave methods, Ceram. Int. 39 (2013) 2283–2292, https://doi.org/10.1016/j.ceramint.2012.08.075.
[76] Y. Chen, W.H. Tse, L. Chen, J. Zhang, Ag nanoparticles-decorated ZnO nanorod array on a mechanical flexible substrate with enhanced optical and antimicrobial properties, Nanoscale Res. Lett. 10 (2015) 106, https://doi.org/10.1186/s11671-014-0712-3.
[77] K. Lim, A. Hamid, M. Azmi, R. Shamsudin, N. Al-Hardan, I. Mansor, W. Chiu, Temperature-driven structural and morphological evolution of zinc oxide nanocoalesced microstructures and its defect-related photoluminescence properties, Materials. 9 (2016) 300, https://doi.org/10.3390/ma9040300.
[78] J. Wang, S. Hou, H. Chen, L. Xiang, Defects-induced room temperature ferromagnetism in ZnO nanorods grown from ε-Zn $(OH)_2$, J. Phys. Chem. C 118 (2014) 19469–19476, https://doi.org/10.1021/jp5058226.
[79] W. Li, L. Fang, G. Qin, H. Ruan, H. Zhang, C. Kong, L. Ye, P. Zhang, F. Wu, Tunable zinc interstitial related defects in ZnMgO and ZnCdO films, J. Appl. Phys. 117 (2015) 145301, , https://doi.org/10.1063/1.4917207.
[80] K. Tang, R. Gu, S. Zhu, Z. Xu, J. Ye, S. Gu, Thermal evolution of zinc interstitial related donors in high-quality NH_3-doped ZnO films, Opt. Mater. Express 7 (2017) 593–605, https://doi.org/10.1364/OME.7.000593.
[81] S. Pal, N. Gogurla, A. Das, S. Singha, P. Kumar, D. Kanjilal, A. Singha, S. Chattopadhyay, D. Jana, A. Sarkar, Clustered vacancies in ZnO: chemical aspects and consequences on physical properties, J. Phys. D Appl. Phys. 51 (2018) 105107, , https://doi.org/10.1088/1361-6463/aaa992.
[82] J.E. Stehr, S.L. Chen, N.K. Reddy, C.W. Tu, W.M. Chen, I.A. Buyanova, Turning ZnO into an efficient energy upconversion material by defect engineering, Adv. Funct. Mater. 24 (2014) 3760–3764, https://doi.org/10.1002/adfm.201400220.
[83] S. Repp, S. Weber, E. Erdem, Defect evolution of nonstoichiometric ZnO quantum dots, J. Phys. Chem. C 120 (2016) 25124–25130, https://doi.org/10.1021/acs.jpcc.6b09108.
[84] H. Kaftelen, K. Ocakoglu, R. Thomann, S. Tu, S. Weber, E. Erdem, EPR and photoluminescence spectroscopy studies on the defect structure of ZnO nanocrystals, Phys. Rev. B 86 (2012) 014113, , https://doi.org/10.1103/PhysRevB.86.014113.
[85] A. Nezamzadeh-Ejhieh, Z. Salimi, Heterogeneous photodegradation catalysis of o-phenylenediamine using CuO/X zeolite, Appl. Catal. A Gen. 390 (2010) 110–118,

https://doi.org/10.1016/j.apcata.2010.09.038.
[86] T. Bora, K.K. Lakshman, S. Sarkar, A. Makhal, S. Sardar, S.K. Pal, J. Dutta, Modulation of defect-mediated energy transfer from ZnO nanoparticles for the photocatalytic degradation of bilirubin, Beilstein J. Nanotechnol. 4 (2013) 714–725, https://doi.org/10.3762/bjnano.4.81.
[87] B. Ohtani, Titania photocatalysis beyond recombination: a critical review, Catalysts 3 (2013) 942–953, https://doi.org/10.3390/catal3040942.
[88] D. Liu, Y. Lv, M. Zhang, Y. Liu, Y. Zhu, R. Zong, Y. Zhu, Defect-related photoluminescence and photocatalytic properties of porous ZnO nanosheets, J. Mater. Chem. A Mater. Energy Sustain. 2 (2014) 15377–15388, https://doi.org/10.1039/C4TA02678K.
[89] J.H. Kim, H.I. Lee, Effect of surface hydroxyl groups of pure TiO_2 and modified TiO_2 on the photocatalytic oxidation of aqueous cyanide, Korean J. Chem. Eng. 21 (2004) 116–122, https://doi.org/10.1007/BF02705388.
[90] I.M.P. Silva, G. Byzynski, C. Ribeiro, E. Longo, Different dye degradation mechanisms for ZnO and ZnO doped with N (ZnO:N), J. Mol. Catal. A Chem. 417 (2016) 89–100, https://doi.org/10.1016/j.molcata.2016.02.027.
[91] G.T.S.T. da Silva, K.T.G. Carvalho, O.F. Lopes, E.S. Gomes, A.R. Malagutti, V.R. Mastelaro, C. Ribeiro, H.A.J.L. Mourão, Synthesis of ZnO nanoparticles assisted by N sources and their application in the photodegradation of organic contaminants, ChemCatChem 9 (2017) 3795–3804, https://doi.org/10.1002/cctc.201700756.
[92] R. Nagaraja, N. Kottam, C.R. Girija, B.M. Nagabhushana, Photocatalytic degradation of rhodamine B dye under UV/solar light using ZnO nanopowder synthesized by solution combustion route, Powder Technol. 215-216 (2012) 91–97, https://doi.org/10.1016/j.powtec.2011.09.014.
[93] J.C. Sin, S.M. Lam, I. Satoshi, K.T. Lee, A.R. Mohamed, Sunlight photocatalytic activity enhancement and mechanism of novel europium-doped ZnO hierarchical micro/nanospheres for degradation of phenol, Appl. Catal. B 148-149 (2014) 258–268, https://doi.org/10.1016/j.apcatb.2013.11.001.
[94] A. Nezamzadeh-Ejhieh, M. Karimi-Shamsabadi, Decolorization of a binary azo dyes mixture using CuO incorporated nanozeolite-X as a heterogeneous catalyst and solar irradiation, Chem. Eng. J. 228 (2013) 631–641, https://doi.org/10.1016/j.cej.2013.05.035.
[95] A. Pavanello, A. Blasco, P.F. Johnston, M.A. Miranda, M.L. Marin, Enhanced photodegradation of synthetic dyes mediated by Ag_3PO_4-based semiconductors under visible light irradiation, Catalysts. 10 (2020) 774, https://doi.org/10.3390/catal10070774.
[96] B. Tatykayev, F. Donat, H. Alem, L. Balan, G. Medjahdi, B. Uralbekov, R. Schneider, Synthesis of core/shell ZnO/rGO nanoparticles by calcination of ZIF-8/rGO composites and their photocatalytic activity, ACS Omega 2 (2017) 4946–4954, https://doi.org/10.1021/acsomega.7b00673.
[97] Y. Xu, M.A. Schoonen, The absolute energy positions of conduction and valence bands of selected semiconducting minerals, Amer. Miner. 85 (2000) 543–556, https://doi.org/10.2138/am-2000-0416.
[98] B. Pal, S. Dhara, P. Giri, D. Sarkar, Room temperature ferromagnetism with high magnetic moment and optical properties of Co doped ZnO nanorods synthesized by a solvothermal route, J. Alloys. Compd. 615 (2014) 378–385, https://doi.org/10.1016/j.jallcom.2014.06.087.
[99] S. Ghattavi, A. Nezamzadeh-Ejhieh, A visible light driven AgBr/g-C_3N_4 photocatalyst composite in methyl orange photodegradation: focus on photoluminescence, mole ratio, synthesis method of g-C_3N_4 and scavengers, Compos. Part B-Eng 183 (2020) 107712, , https://doi.org/10.1016/j.compositesb.2019.107712.
[100] J. Kou, C. Lu, J. Wang, Y. Chen, Z. Xu, R.S. Varma, Selectivity enhancement in heterogeneous photocatalytic transformations, Chem. Rev. 117 (2017) 1445–1514, https://doi.org/10.1021/acs.chemrev.6b00396.
[101] N. Omrani, A. Nezamzadeh-Ejhieh, A comprehensive study on the mechanism pathways and scavenging agents in the photocatalytic activity of $BiVO_4$/WO_3 nano-composite, J. Water Process Eng 33 (2020) 101094, , https://doi.org/10.1016/j.jwpe.2019.101094.